

Linking drainage front morphology with gaseous diffusion in unsaturated porous media: A lattice Boltzmann study

Jessica Furrer Chau*

Dept. of Civil and Environmental Engineering, University of Connecticut, Storrs, Connecticut 06269, USA

Dani Or†

*Laboratory of Soil and Environmental Physics (LASEP), School of Architectural, Civil and Environmental Engineering (ENAC/ISTE),
Ecole Polytechnique Federale de Lausanne (EPFL), Lausanne, Switzerland*

(Received 21 April 2006; revised manuscript received 6 September 2006; published 13 November 2006)

The effect of drainage front morphology on gaseous diffusion through partially saturated porous media is analyzed using the lattice Boltzmann method (LBM). Flow regimes for immiscible displacement in porous media have been characterized as stable displacement, capillary fingering, and viscous fingering. The dominance of a flow regime is associated with the relative magnitudes of gravity, viscous, and capillary forces, quantifiable via the Bond number Bo , capillary number Ca , and their difference, $Bo - Ca$. Forced drainage from an initially saturated two-dimensional (2D) porous medium was simulated and the resulting flow patterns were analyzed and compared with theoretical predictions and experimental results. The LBM simulations reproduced expected flow morphologies for a range of drainage velocities and gravitational forces (i.e., a range of capillary and Bond numbers). Furthermore, measures of drainage front width as a function of the dimensionless difference $Bo - Ca$ correspond well with scaling laws derived from percolation theory. Effects of flow morphology on residual fluid entrapment and gaseous diffusion were assessed by running LBM diffusion simulations through the partially saturated domain for a range of water contents. The effective diffusion coefficient as a function of water content was estimated for three regimes: stable drainage front, capillary fingering, and viscous fingering. Significant reductions in gaseous diffusion coefficient were found for viscous fingering relative to stable displacement, and to a lesser extent for capillary fingering, indicating that wetting phase distribution with a high degree of fingering in the 2D domain severely restricts connectivity of gas diffusion pathways through the medium. The study lends support for the use of LBM in design and management of fluids in porous media under variable gravity, and enhances the understanding of the role of dynamic fluid behavior on macroscopic transport properties of partially saturated porous media.

DOI: [10.1103/PhysRevE.74.056304](https://doi.org/10.1103/PhysRevE.74.056304)

PACS number(s): 47.56.+r, 68.03.-g, 89.75.Da, 47.20.-k

I. INTRODUCTION

The study of immiscible displacement in porous media is of considerable interest for many hydrological, industrial, and engineering applications, involving flow processes at scales ranging from pore to field scale. Analytical and numerical simulations of flow processes at the pore scale provide insights into the impact of dynamic flow conditions (e.g., displacement front configuration) on mesoscopic or macroscopic transport properties of the system in ways that would not be possible in a physical experiment such as a micromodel. In this study, we use the lattice Boltzmann method (LBM) to quantify the effects of displacement front morphology on a macroscopic transport process of the porous medium, namely the effective diffusion coefficient in the gas phase. Gas diffusion in porous media is well-understood for uniform liquid distribution, but the effects of nonuniform wetting such as that caused by fingering during immiscible displacement is unknown. The morphology of the displacement front reflects influences of various factors including displacement velocity, viscosity ratio of the fluids,

pore size distribution, and gravity. In this work, we show that these factors have an indirect but important effect on gas diffusion as well, through their effects on the displacement front.

This work was motivated by questions concerning two-phase flow in porous media under reduced gravity relevant to design and fluid management in plant-growth modules for use in microgravity conditions (i.e., aboard the International Space Station), and potentially to a broader class of related issues such as linking liquid behavior to gaseous fluxes in fuel cells and unsaturated soils.

Our study was conducted in two parts. We first simulated drainage in a two-dimensional porous medium using the LBM under a range of drainage velocities and gravitational accelerations, and quantified the resulting flow morphologies. We subsequently simulated gas diffusion through the drained medium and plotted the measured effective diffusion coefficient as a function of mean water content for three morphologies: stable displacement, capillary fingering, and viscous fingering. We show that flow morphology has a significant effect on the magnitude of gas diffusion that can occur through a porous medium.

II. THEORETICAL BACKGROUND

We provide a brief overview of the extensive body of work devoted to immiscible flow in porous media in Sec.

*Email address: chau@engr.uconn.edu†Author to whom all correspondence should be addressed. Email address: dani.or@epfl.ch

II A, followed by a discussion of gaseous diffusion in porous media in Sec. II B. Sec. II C contains a brief introduction to the lattice Boltzmann method.

A. Theory of immiscible flow in porous media

We focus on drainage in porous media, in which a wetting fluid (fluid 1, or the defending fluid) is displaced by a non-wetting fluid (fluid 2, or the invading fluid). Depending on the conditions of displacement, different flow regimes may be observed. Stable displacement occurs when the front between the two fluids is flat, or when the front width (distance between the most and least advanced portion of the front) is constant with time. Destabilizing influences such as large viscosity ratio, action of gravity, or rapid drainage velocities can cause the front width to grow without bound, resulting in instability and the onset of fingering.

1. Dimensionless numbers Ca and Bo

To quantify the relative importance of various driving forces in our flow domain, we employ the dimensionless capillary (Ca) and Bond (Bo) numbers, which summarize the relative importance of primary forces and properties that control two-phase flow in porous media and are given by

$$Ca = \frac{\mu V a^2}{\sigma \kappa} = \frac{\rho \nu V a^2}{\sigma \kappa}, \quad (1a)$$

$$Bo = \frac{\Delta \rho g a^2}{\sigma}, \quad (1b)$$

where $\mu = \rho \nu$ is fluid dynamic viscosity, ν is kinematic viscosity, V is fluid velocity, ρ is fluid density, σ is surface tension, κ is the intrinsic permeability of the porous medium, a is the average pore radius, $\Delta \rho$ is the density difference between the two fluids, and g is the acceleration due to gravity.

Ca quantifies the relative importance of viscous and capillary forces. The strength of capillary forces in a porous medium is dependent on the surface tension, which in turn depends on the contact angle formed at fluid contacts with the solid surfaces. The other factor defining the strength of capillary forces is the pore throat radius where the critical pressure for invasion of the wetting fluid filled pore by the nonwetting fluid is inversely proportional to the radius,

$$P_c = \frac{2\sigma \cos \gamma}{r}. \quad (2)$$

For $Ca \ll 1$, capillary forces are dominant and local variations in pore throat size govern the flow path. The nonwetting phase advancing on several pore throats will invade the largest pore first where the critical pressure is lowest. Once that pore has been drained, a new set of pore throats presents itself to the invading front, and the process repeats. This process is well-described by the invasion percolation (IP) algorithm [1]. For $Ca \gg 1$, viscous forces are significant relative to capillary forces, and viscous fingering can occur. An analysis of forces in this regime is discussed in Sec. II A 2. At intermediate Ca , a crossover regime has been observed,

exhibiting fluid behavior with characteristics of both regimes [2].

Bo quantifies the relative magnitude of gravitational and capillary forces. For $Bo \ll 1$, capillary forces dominate and IP-like behavior can be expected. For $Bo \gg 1$, gravity is the most significant force. In the case of vertical drainage in natural systems, gravity acts on the water phase and serves as a stabilizing force by flattening the interface and eliminating height differences caused by viscous instability or capillary fluctuations.

2. Mechanisms of viscous instability

Homsy [3] provides a definitive analysis of the mechanisms of viscous instability in porous media (attributed to Hill [4]), as well as some illustrative examples. Assuming that flow in porous media satisfies Darcy's law, the pressure drop across an interface is given by

$$\Delta p = p_2 - p_1 = \left[(\mu_1 - \mu_2) \frac{U}{k} + (\rho_2 - \rho_1) g \right] \Delta x, \quad (3)$$

where the subscript 1 indicates a parameter of the defending fluid and 2 represents the invading fluid, U is the velocity of invasion (average interstitial fluid velocity), and k is intrinsic permeability. A positive value of Δp causes any perturbation of the invading front (due to nonuniformity of the medium) to grow, resulting in viscous instability. In the case of vertical drainage, where $\mu_1 - \mu_2 > 0$ and $\rho_2 - \rho_1 < 0$, gravity has a stabilizing influence and viscosity contrast has a destabilizing one. When $g = 0$ (horizontal flow or microgravity conditions), viscosity contrast is the only destabilizing influence, and the invasion velocity controls the magnitude of the instability.

For the case of air invading a water-saturated medium horizontally or under microgravity, an intuitive explanation for the viscous fingering phenomenon is as follows: water is removed from the outlet of the saturated medium at a prescribed rate that induces advancement of the drainage front (air invasion) into the medium. In the absence of restraining gravity force and for high drainage velocities, the liquid is forced to evacuate the medium through the most conductive pathways available (largest pore spaces). Quick withdrawal limits opportunity time for interfacial reconfiguration (spreading induced by capillarity), resulting in a smaller liquid-gas interfacial area than with other displacement modes. This process creates the thin branching fingers described by studies of viscous fingering in porous media [2,5–7].

3. Flow regimes

Numerous studies have focused on identifying key factors governing flow morphology of immiscible displacement in porous media. A comprehensive review by Chen *et al.* [8] summarizes the conditions under which unstable fronts develop, including flow field orientation, fluid characteristics such as viscosity ratio and density, and characteristics of the porous medium such as permeability, heterogeneity, prewetted condition, and water repellency.

For immiscible displacement, three main flow regimes have been identified [2]. The corresponding front morpholo-

gies exhibit specific characteristics that are quantifiable via measurement of fractal dimension. Capillary fingering morphology is produced by a flow regime in which capillary forces are dominant ($Ca \ll 1$); therefore, pores are filled by sequential invasion of the largest pore, regardless of primary flow direction. These conditions produce a wide front with trapping of the wetting phase at a range of scales [1,2]. Viscous fingering results when viscous forces are significant ($Ca \gg 1$) and exhibits thin loopless branched fingers that grow primarily in the flow direction [2,6].

Early work by Lenormand *et al.* [2] investigated the effects of Ca and viscosity ratio $M = \mu_1/\mu_2$ on flow morphology using computer simulations and etched glass networks. Neglecting gravitational effects, they performed drainage experiments at several values of Ca and M , and produced a phase-space diagram delineating parameter domains for stable displacement, capillary, and viscous fingering. They also observed “crossover” behavior in intermediate regions of their phase-space diagram corresponding to flow morphologies with characteristics of more than one regime. The flow patterns in their study were identified “by eye” and were not based on quantitative analysis of the front morphology. Berkowitz and Ewing [9] expanded Lenormand *et al.*’s phase-space diagram to include gravitational effects by including Bo as a third dimension.

Meheust *et al.* [10] used 2D glass bead packs to study drainage morphology for a range of Ca and Bo values. They defined a “generalized Bond number” $Bo^* = Bo - Ca$ and showed that experimental drainage front morphology was a function of Bo^* . For $Bo^* > 0$, indicating $Bo > Ca$, the predominance of gravitational forces resulted in stable displacement (flattened fronts). For $Bo^* < 0$ or $Ca > Bo$, the diminishing stabilizing force produced fronts that became progressively more unstable, indicated by increasing front width as Bo^* became more negative. At slightly negative Bo^* values (in the range of $0 < Bo^* < -0.05$), capillary forces became significant, resulting in behavior characteristic of capillary fingering. As Bo^* decreased further, viscous forces became significant and viscous fingering was observed for values of $Bo^* < -0.08$ (approximate range). These experimental results provide useful benchmarks for comparison with the results of our LBM simulations in a simplified porous medium.

4. Scaling of front widths for stable fronts

Meheust *et al.* [10] invoked arguments based on percolation theory to derive a scaling law quantifying the behavior of stable fronts (where $Bo^* > 0$). Briefly, they developed an expression relating the capillary pressure in any pore in the wetting fluid as a function of the sum of the average pressure drop (hydrostatic and viscous pressure gradients) and a uniformly distributed pressure term related to the pore size distribution. They also defined a dimensionless “fluctuation number” F quantifying the ratio between the average pressure drop over pores and the capillary threshold pressure fluctuations in the porous medium. By estimating the frequency of the percolation capillary threshold pressure as $1/W_i$, where W_i is the width of the normalized capillary threshold pressure distribution, they related the front width to

W_i and the generalized Bond number Bo^* using the following expression:

$$w \sim F^{-\nu/(1+\nu)} = \left(\frac{\sigma}{W_i a} Bo^* \right)^{-\nu/(1+\nu)}, \quad (4)$$

where w is the width of the wetting front, σ is the surface tension, a is the average pore size, and ν is the percolation correlation length exponent, equal to $4/3$ for 2D systems. This equation provides a theoretical prediction against which to measure the behavior of stable wetting fronts as a function of generalized Bond number. It predicts an exponential decrease in front width as Bo^* increases (i.e., as gravity becomes more significant), with the value of the exponent equal to $(-4/3)(1+4/3) \approx -0.571$.

5. Characterization of flow patterns for unstable fronts

A large body of literature focuses on the characterization of flow patterns in porous media using fractal geometry. The principle behind this approach is that many patterns in natural systems exhibit statistical self-similarity; that is, they have some property that is statistically invariant over a wide range of scales. Capillary fingering patterns, for example, exhibit clustering and phase trapping over a range of scales. The simplest and most intuitive way of calculating fractal dimension is the box-counting method, in which (in 2D space) the object of interest is covered by squares/boxes of varying sizes. A power-law relationship exists between the number of boxes necessary, N , and the side length L of the box. That is,

$$N \sim L^{-D}, \quad (5)$$

where D is defined as the fractal dimension. The fractal dimension is determined from the slope of a $\log(L) - \log(N)$ plot. For a Euclidean object (e.g., a straight line or rectangle), the exponent obtained from such a plot would be an integer; a fractal object would exhibit a nonintegral exponent.

The concept of fractal dimension has been employed in the study of flow in porous media to characterize and distinguish between different displacement regimes and front morphology. Several studies have drawn analogies between the flow patterns formed by capillary fingering in porous media and invasion percolation [1,11], and between viscous fingering and diffusion-limited aggregation (DLA) [5–7]. The patterns generated by IP and DLA have specific fractal dimensions associated with them, which are consistent with measured fractal dimensions of the corresponding flow patterns in porous media. It is now commonly accepted that viscous fingering patterns in porous media are characterized by a typical fractal dimension $D_f \sim 1.62$ while capillary fingering patterns are characterized by $D_f \sim 1.82$.

B. Gas diffusion in porous media

Gas diffusion in an unsaturated porous medium takes place through the interconnected air-filled pore spaces of the medium. Quantification of this process is accomplished by measuring a macroscopic effective diffusion coefficient that

varies with the porosity and degree of saturation. The effective diffusion coefficient through a soil sample is measured experimentally by fixing the concentration at each end of the sample (thereby prescribing the concentration gradient), and measuring the steady-state diffusive flux through the sample [12]. A macroscopic application of Fick's law is then employed to determine the effective diffusion coefficient,

$$J = -D_{\text{eff}} \frac{\Delta C}{\Delta z}. \quad (6)$$

Several models have been developed to describe the dependence of the effective gaseous diffusion coefficient on water content in soils and other porous media. In a previous study [13], we provided a brief review of such models and used one to describe LBM experiments of gas diffusion at varying water contents, namely the Penman-Millington-Quirk model [14],

$$D_{\text{rel}} = 0.66\Phi \left(\frac{\varepsilon}{\Phi} \right)^{(12-m)/3}, \quad (7)$$

where Φ is porosity, ε is air-filled porosity, and m is a fitting parameter. Moldrup *et al.* [14] tested this model for sieved, repacked soils and found $m=6$ to give the best fit. Soil water contents were obtained by placing the soil samples in contact with water and allowing them to imbibe the desired liquid mass, thus ensuring that the water was uniformly distributed within the soil samples. It is important to note that uniform distribution is an important condition for the validity of macroscopic models like Eq. (7). Conditions of nonuniform wetting such as those investigated in this study introduce complexities not considered by such models.

C. Lattice Boltzmann method

The lattice Boltzmann method (LBM) is a well-established platform for studying fluid dynamics in a variety of contexts, and there is an extensive body of literature devoted to it. Therefore, we provide only a cursory description here and refer interested readers to [15,16] for a full exposition of the method, and to [13,17–21] for examples of applications for which it has been utilized.

1. LBM code development and testing

The LBM involves distributions of particles on a two- or three-dimensional lattice which undergo streaming (advection toward neighboring grid locations) and collisions. The effect of collisions is that particle distributions relax at each time step toward equilibrium given by a Maxwellian distribution. Mesoscopic fluid parameters (density and velocity) are calculated from the particle distributions at each grid point at each time step.

Our two-component lattice Boltzmann code uses a square 2D lattice, and our implementation follows the method outlined by Shan and Chen [15]. However, we have combined the Shan-Chen model with the gravity implementation derived by Luo [16], which to the best of our knowledge is a novel approach. This is an improvement over the Shan-Chen gravity implementation because g , the acceleration due to

gravity, is incorporated into a rigorously derived external force term in the lattice Boltzmann equation. In contrast, the Shan-Chen method implements gravity as a modification to the fluid mesoscopic velocity. Luo's [16] implementation allows the value of g to be used directly in calculations of dimensionless numbers (Ca and Bo) and in the Poiseuille flow analysis described below.

We ran several preliminary tests of our LB code, both to verify that it adequately reproduced fluid dynamics and to determine numerical values for the fluid parameters of interest (surface tension σ and kinematic viscosity ν). The surface tension value between the two fluids is typically determined using the Laplace law for 2D,

$$\Delta P = \frac{\sigma}{R}, \quad (8)$$

where R is the radius of a bubble of one fluid in the other, and ΔP is the pressure difference between the inside and outside fluids (determined from the density difference $\Delta\rho$ using the ideal-gas equation of state $P=\rho/3$) [22]. Plotting $1/R$ versus ΔP and fitting a line to the data gives an estimate of σ [Fig. 1(a)].

The LB fluid with relaxation parameter $\tau=1$ has a theoretical value of kinematic viscosity $\nu=1/6 \text{ lu}^2 \text{ ts}^{-1}$ [16]. We verified this in our code by simulating Poiseuille flow between parallel plates and comparing the fully developed velocity profile to the analytical solution [23]

$$V(x) = \frac{1}{2\nu\rho} \left(\frac{dP}{dy} \right) (x^2 - h^2), \quad (9)$$

where ν is the kinematic viscosity, ρ is the fluid density, h is half the gap width, and $dP/dx=\rho g$ is the pressure gradient in the x direction (gravity-driven flow). Parameters h and g are prescribed in the code and $V(x)$ is an output. Therefore only ν is unknown, allowing for comparison with the theoretical value. The theoretical value of $1/6$ results in a perfect match between observations and the analytical solution [Fig. 1(b)].

The difference between the velocity profiles of the wetting and nonwetting fluids in Fig. 1(b) is a numerical effect due to a difference in apparent wall position for the two boundary implementations (the effective channel width is less for the wetting fluid). It is well known that simple bounce-back or “no-slip” boundary conditions result in an effective wall position of halfway between the fluid and solid nodes [24]. Although other studies make reference to changes in effective wall position (e.g., in the presence of second-order velocity derivatives [25]), none specifically mentions the contrast between the wetting and nonwetting fluid, which we present here. Our results show that implementation of fluid-solid interaction (wetting) results in a further reduction in the effective width of the channel by an additional $1/6 \text{ lu}$. This implies that for the same pressure drop, the wetting fluid would achieve a lower velocity in a given channel, which is similar to the effect that an increase in viscosity would have. Therefore, there is a slight ($\sim 10\%$) apparent viscosity contrast between our wetting and nonwetting fluids.

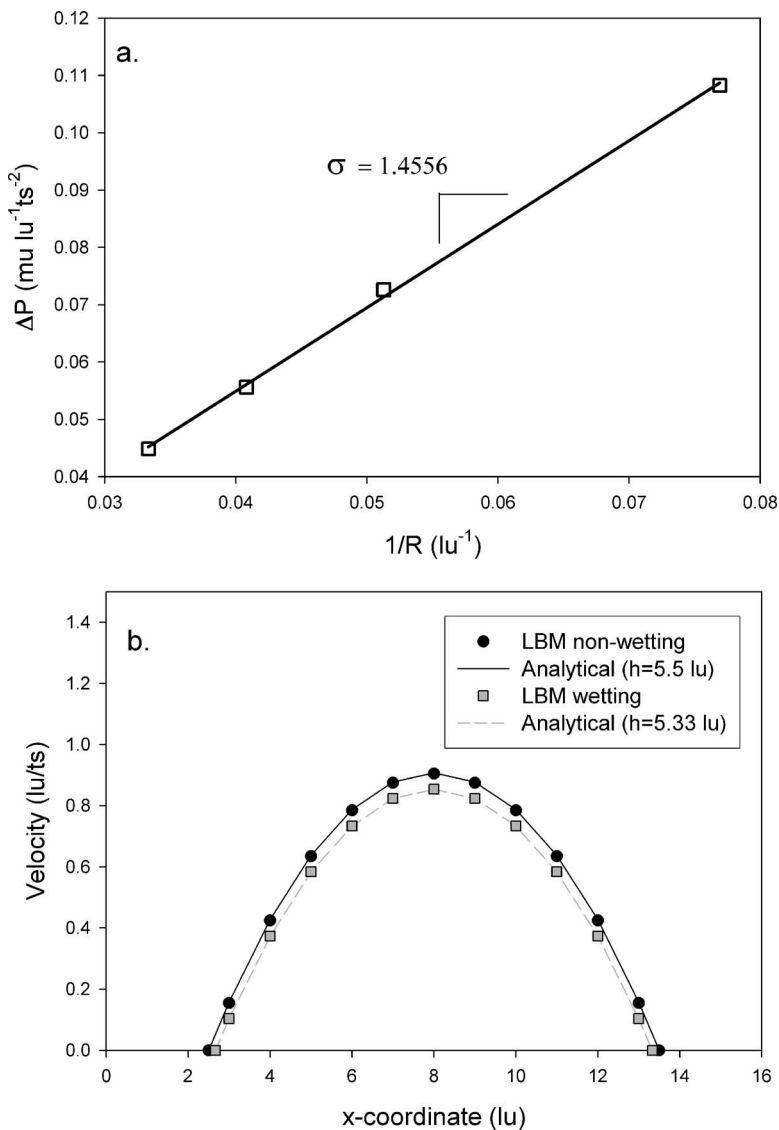


FIG. 1. (a) Plot of $1/R$ vs ΔP for bubbles of various sizes. The slope of the fitted line gives a value for σ , the fluid surface tension. (b) Measured velocity profiles in the same channel for a fluid with wetting parameter=0 and >0 . Fitting the velocity distributions to Eq. (9) gives an estimate of fluid viscosity. Units are lu , lattice units (length); ts , time steps; μ , mass units.

2. Testing of LBM fluid dynamics

Preliminary tests of the dynamics of the two-fluid system employed liquid slugs in capillary tubes falling under the influence of gravity. Several sources [10,26–28] suggest the presence of scaling laws between Ca and Bo of such a system. According to Podgorski *et al.* [26], the Bond number of such a system should scale linearly with the capillary number above a critical value of the Bond number, Bo_{\min} , which represents the magnitude of capillary pinning force. (Bo_{\min} is the value below which the slug velocity is zero.) For slugs of varying lengths (10, 14, and 25 lattice units), we applied varying gravitational forces and measured the fall velocity. The result was three highly linear plots with positive Bo intercepts whose slopes increased with slug length L (only two plots are shown in Fig. 2 for clarity).

Next, we compared our simulation results to experimental data from Bico and Quere [28], Podgorski *et al.* [26], and Or and Ghezzehei [27]. The Or and Ghezzehei data were calculated from experimental results of Su *et al.* [29], which examined the flow of slugs of water between parallel plates. Bico and Quere [28] performed experiments of slugs falling

in round capillary tubes in order to quantify the maximum velocity as a function of slug length. We calculated Ca and Bo for each of their experiments using their published data. Podgorski *et al.* [26] measured the sliding velocity of liquid droplets on inclined planes, and reported much smaller Ca values than other studies, including this one (hence the seemingly flat line in Fig. 2). The reason for the order-of-magnitude difference in slope is their use of an alternate, and more generic, definition of the capillary number,

$$\text{Ca} = \mu V / \sigma, \quad (10)$$

which does not include the geometry-specific permeability factor k , to be discussed further in the next paragraph.

Some discussion of the slopes shown in Fig. 2 is in order. As postulated by Podgorski *et al.* [26], Ca can be expressed as a linear function of Bo as follows:

$$\text{Ca} = m(\text{Bo} - \text{Bo}_{\min}), \quad (11)$$

where m is some constant value of the slope and Bo_{\min} is the critical value of the Bond number to induce motion as discussed above. Since Bo_{\min} is small, we can approximate

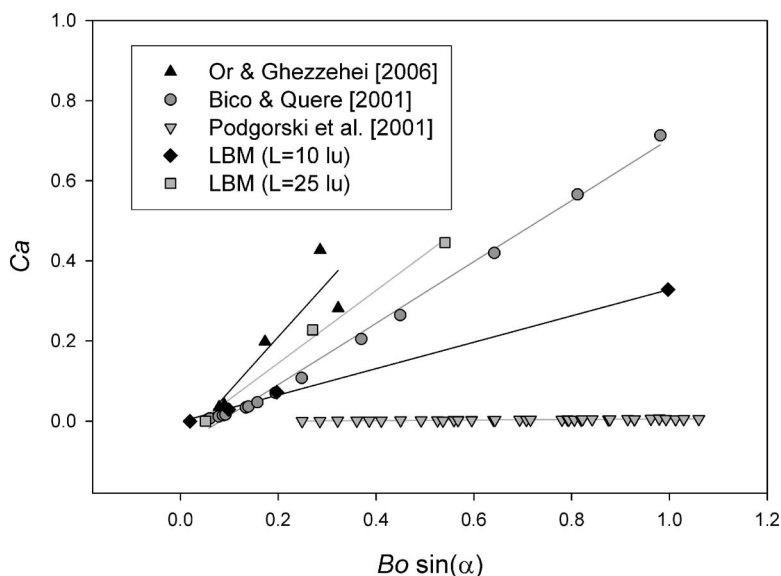


FIG. 2. Scaling of Ca with Bo for LBM simulations and experimental results from the literature. (α =angle of inclination of experimental geometry, giving vertical component of gravity.) LBM simulations were of liquid slugs of length L falling under gravity in 2D capillary tubes.

$$m \approx \frac{Ca}{Bo} = \frac{\mu V 1}{\rho g k} \quad (12)$$

using Ca and Bo as defined in Eqs. (1a) and (1b). The first factor in Eq. (12) quantifies the balance between viscous and gravitational forces, while the second is the inverse of a geometry-specific permeability parameter with units of length squared. The value of k is well known for some specific geometries: it equals $b^2/12$ for a fracture of aperture $2b$, $r^2/8$ for a capillary tube of radius r , and so on. This permeability factor contributes to the different slopes observed in Fig. 2. The different experimental geometries exhibit different permeabilities, reflecting the different mechanisms of viscous dissipation of energy as the liquid falls under gravity. However, our LBM results for different slug lengths show that permeability is not the sole determining factor of Ca – Bo slope; fall velocity variations resulting from dynamic contact angle effects [28] are also important. These effects may explain the scatter in the experimental results shown in Fig. 2. The observed slopes of the Ca – Bo plots vary from experiment to experiment. Bo_{\min} , however, is a dimensionless parameter that identifies the crossover between liquid pinning by capillary forces and motion caused by gravity. This value should be relatively constant for all systems, and the LB data show very good agreement with experimental results.

III. SIMULATION METHODS

A. LBM drainage simulations

Drainage simulations were performed in a computer-generated 2D porous medium at a range of Bo^* ($=Bo-Ca$) values. The domain was initially filled with a wetting fluid (visualized as blue), with a thin strip of nonwetting fluid (visualized as white) at the top. The properties of the fluids were identical, except that the wetting fluid had a contact angle of approximately 0° with the solid. Also, the apparent viscosities of the two fluids were different, as described in Sec. II C 1. Periodic (wrap-around) boundaries were applied

at the sides of the domain. Ca was prescribed by setting the fluid velocity along the top and bottom boundaries of the simulation, in the range of 0.0005–0.02 lu/ts (lattice units per time step). Bo was prescribed by setting the gravitational acceleration, in the range of 0–0.002 lu/ts² for the wetting fluid. In order to compensate for the identical densities of the wetting and nonwetting fluids, the gravitational acceleration applied to the nonwetting fluid was three orders of magnitude lower than that applied to the wetting fluid. Accordingly, Bo was defined as

$$Bo = \frac{\Delta(\rho g)a^2}{\sigma}, \quad (13)$$

in contrast to the standard definition given in Eq. (1a), which assumes that g is constant and that the density difference between the fluids determines the magnitude of the gravitational force.

B. Porous medium generation

The porous medium was generated by placing circles of varying radius in a 600×600 pixel domain. Each pixel corresponded to one lattice spacing in the LB code. Circle centers were chosen from a uniform distribution and circle radii from a normal distribution $N(8, 2)$. A minimum spacing of two pixels was set so that the circles would not overlap. The porosity of the domain was $n=0.7$. Lower porosities in the range of 0.55–0.65 were attempted, but these simulations resulted in numerical instabilities at high flow velocities. A high porosity is necessary to maintain connected flow paths between particles in this 2D representation of a porous medium; a 3D representation could sustain flow at a lower porosity because of the connectivity in the third dimension. Therefore, the high porosity is an artifact of the dimensionality of the system. Other ramifications of the 2D nature of the simulations will be discussed later in the text.

C. Image processing and calculation of fractal dimension

The LB fluid density data from each simulation were imaged using a blue color scale corresponding to the density of

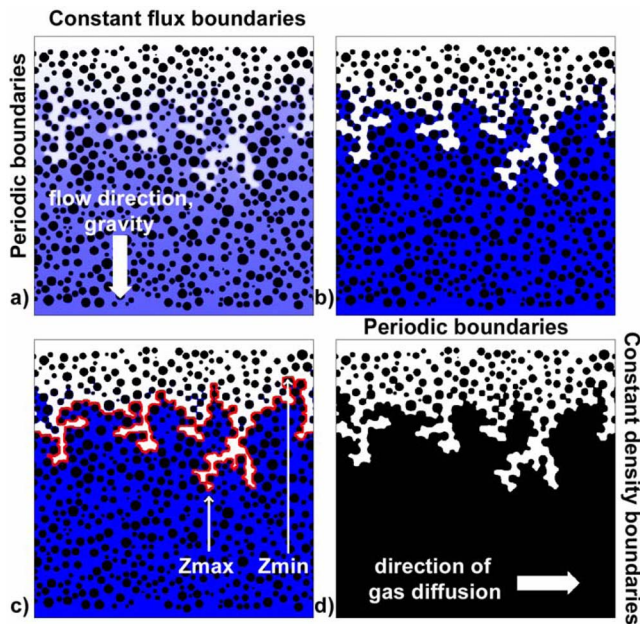


FIG. 3. (Color online) Modification of LBM results for various purposes: (a) original bluescale image, (b) thresholded image for extraction of front points, (c) front points shown in red (used to calculate fractal dimension), (d) black/white image for diffusion simulation.

the wetting fluid [Fig. 3(a)]. The images were then processed using a threshold density to produce an image in which gas nodes were pure white, liquid nodes were pure blue, and solid nodes were black [Fig. 3(b)]. Then the points on the boundary between air and the other phases were extracted [Fig. 3(c)] and used to calculate the fractal dimension of the front.

A box-counting algorithm was employed to calculate the fractal dimension, following Lenormand and Zarcone [1]. The origin for the boxes was located in the middle of the domain, except in instances where the front did not coincide with this point. Then the origin was moved closer to the front

in order to avoid the anomalous results described by Lenormand and Zarcone (in which origins outside the radius of gyration produced different calculated fractal dimensions). Box length L and the resulting number of front points N inside the box were plotted on a log-log scale, with the fractal dimension given by the slope of the plot. That is, the fractal dimension D is given by the scaling law

$$N \sim L^D. \quad (14)$$

The plots were linear for $L > \sim 10$ lattice units. [See Fig. 4 for a typical $\log(N) - \log(L)$ plot.]

D. LBM gas diffusion simulations

In the second phase of our experiment, we used the results from the drainage simulations and converted each liquid node to a solidlike node, creating a new domain wherein both solids and liquids were impervious to gas diffusion [Fig. 3(d)], that is, $D_{\text{gas-solid}} = D_{\text{gas-liquid}} = 0$. We then simulated gas diffusion through the air-filled portion of the medium using a multicomponent lattice Boltzmann code in which the fluid-fluid interaction parameter was set to zero (i.e., no fluid-fluid attraction or repulsion).

Gas diffusion experiments were run horizontally (in the direction transverse to gravity) through the converted domains using periodic (wrap-around) boundaries on the sides parallel to the diffusive flux and constant density (concentration) boundaries on the sides of the domain perpendicular to the diffusive flux. The effective diffusion coefficients across the domain were calculated using Fick's law as described in Sec. II B. Our methodology is described in more detail by Chau *et al.* [13].

In the context of plant growth modules for use in microgravity conditions, this experimental setup corresponds to the following physical scenario: a plant growth module is launched dry, then flushed with an aqueous solution and drained to a prescribed water content suitable for plants. In the management of the fluid, uniform wetting is assumed, and oxygen is allowed to diffuse through the root zone. Our

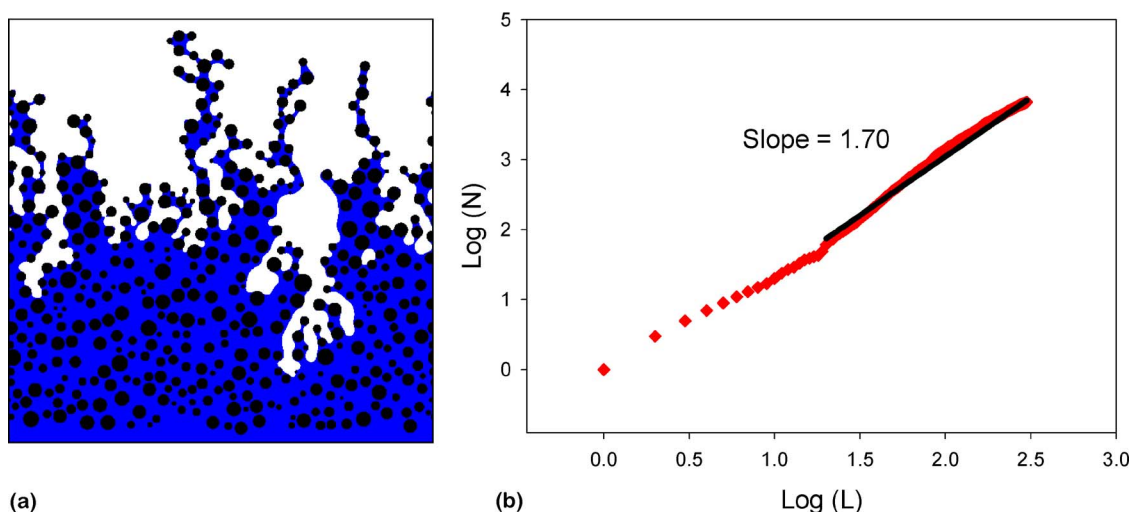


FIG. 4. (Color online) (a) Final image before breakthrough for simulation with $\text{Bo}^* = -0.12$ (thresholded, trapped solids removed). (b) Box-counting plot for determination of fractal dimension according to Eq. (14), using all points bordering blue and white regions in (a).

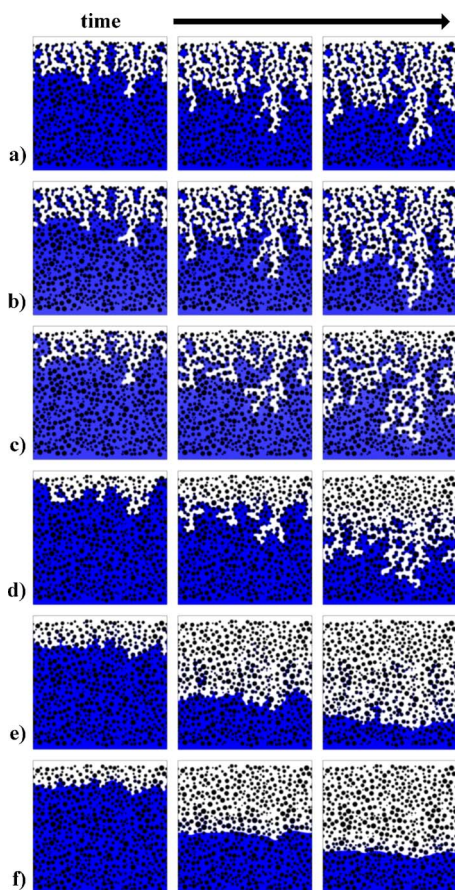


FIG. 5. (Color online) Time series for selected simulations. Bo^* values are (a) -0.12 , (b) -0.06 , (c) -0.008 , (d) -0.006 , (e) 0.04 , (f) 0.15 . Bo^* values are obtained by varying gravity and inlet velocity. Increase in the stability of the interface (flatness of the front) is observed with increasing Bo^* . All images are thresholded (nodes designated as air or water according to a threshold density).

simulations show that drainage conditions would have a significant effect on actual liquid configuration within the module, and that knowledge of the flow regime is very important in predicting the magnitude of the diffusive gas flux in such a system.

IV. RESULTS

A. Scaling of front behavior with Bo^*

1. Fractal dimension of the front

Figure 5 shows time series of drainage simulations for all Bo^* values. For $Bo^* < 0$ (i.e., $Ca < Bo$), all simulations exhibited fingering. As Bo^* increased above zero, fronts became successively flatter (more stable). At low Bo^* ($Bo^* \leq -0.05$), the fingers observed had similar characteristics to those attributed to viscous effects in other studies (thin loopless branched fingers that grow primarily in the flow direction) [2,6]. Fractal dimensions of the fronts points [denoted by the red line in Fig. 3(c)] were consistent with the viscous fingering regime ($1.65 < D_f < 1.7$).

For Bo^* between ~ -0.01 and 0, the evolution of the front was qualitatively similar to capillary fingering/IP behavior.

Sequential invasion of the largest pore spaces (independent of flow direction) and trapping of liquid clusters in smaller pore spaces were observed. Fingers were wider than those observed at low negative Bo^* . When the fractal dimension of the front [red points in Fig. 3(c)] was calculated, it was lower than the characteristic value of 1.82 [1,11] for capillary fingering fronts ($D_f = 1.63$). However, calculating the fractal dimension of the air-filled region [all white points above the red line in Fig. 3(c)] gave results in good agreement with the characteristic value ($1.85 < D_f < 1.86$).

The inconsistency in fractal dimension exhibited by the two types of fronts may be related to the 2D nature of the simulations. As mentioned earlier, particles in the porous medium had to be widely spaced to allow flow between them, resulting in thicker fingers than would be observed if the particles were more tightly packed. Viscous fingering morphologies in real porous media are characterized by thin branching fingers, of that the outlines of the LBM fingers are a good topological approximation. On the other hand, capillary fingering morphologies exhibit more consolidated fingers that are better approximated by the space-filling air-invaded region in our simulations. For both methods of calculation, the results for the capillary fingering and viscous fingering domains were different enough to be significant (at least 0.2 difference).

Simulation scale may also contribute to the inconsistency in calculated fractal dimension. Other studies of fingering behavior have used networks or micromodels with dimensions of 400–500 pore spaces/bonds [1,10]. Due to the scale of the LBM simulations, the largest network that can be simulated in a reasonable amount of time is on the order of 100 pore sizes. Therefore, there is some difficulty in measuring the fractal dimension of the results with the same metric as is used for closer approximations of real porous media (e.g., glass beads).

2. Front width behavior

To further characterize the differences between the flow regimes, we analyzed the behavior of the front width, defined here as the vertical distance between the most and least advanced point on the front, for several simulations. The most advanced point on the front is denoted with vertical coordinate z_{\max} , the least advanced point has coordinate z_{\min} , and $\Delta z = z_{\max} - z_{\min}$. Front width evolution (Δz versus time) for all simulations with $Bo^* > 0$ are shown in Fig. 6(a). Simulations at different Bo^* values within the viscous fingering regime had nearly identical front width evolution patterns, while a different pattern emerged for simulations in the capillary fingering and crossover regimes.

For the two viscous fingering simulations ($Bo^* = -0.12$ and -0.06), Δz increased linearly with time. Remarkably, in spite of having different inlet fluxes, both simulations exhibited a slope of three times the inlet flux for the Δz versus time plot. Other simulations exhibited different “characteristic” slopes. This phenomenon has not, to our knowledge, been discussed in the literature, with the possible exception of Maher [6], who observed a power-law relationship between the dimensionless length of the mixing zone and dimensionless time. To explore the physical basis for these

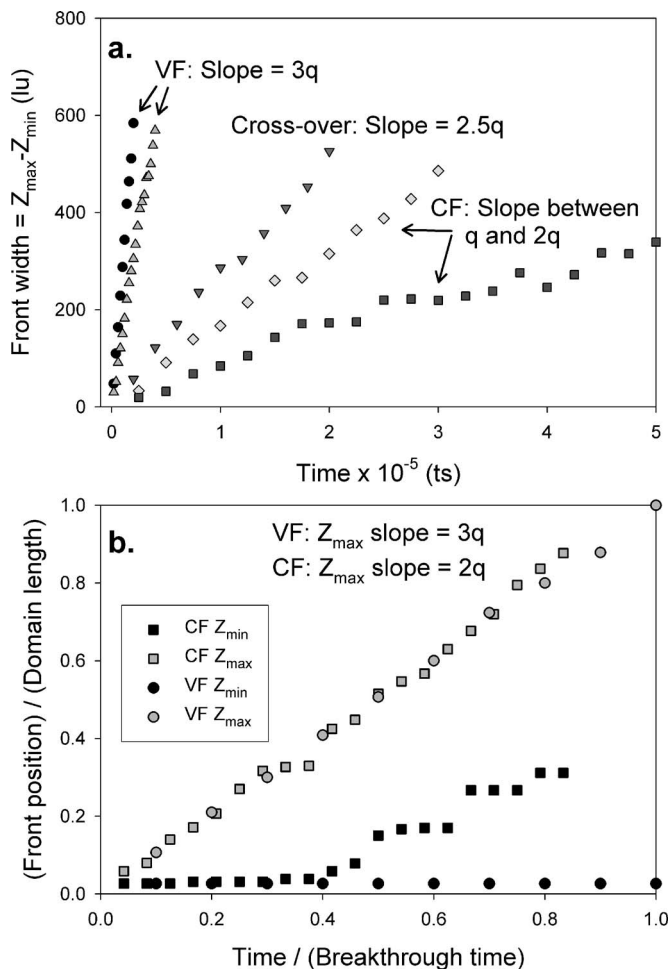


FIG. 6. (a) Front width ($z_{\max} - z_{\min}$) evolution for all simulations with unstable fronts ($Bo^* < 0$). Different flow morphologies yield different characteristic slopes. (b) Dimensionless evolution of z_{\min} and z_{\max} for two limit cases (viscous fingering and capillary fingering). The CF and VF curves in part (a) are given by the difference between the z_{\max} and z_{\min} curves in part (b). Units are lu, lattice units (length); ts, time steps.

characteristic slopes, we plotted z_{\max} and z_{\min} separately [shown in Fig. 6(b)] for two limit cases—highest and lowest negative Bo^* values].

For the viscous fingering case, flow occurred mainly in the foremost finger while liquid configurations in other parts of the domain remained relatively stagnant. Z_{\min} did not move throughout the simulation, indicating that a portion of the front remained pinned at the inlet. The most advanced point on the front (the tip of one dominant finger) moved downward at almost exactly three times the prescribed flux rate of the system, indicating that flow was occurring there at the expense of the advancement of other portions of the front. Therefore, the slope of the Δz versus time plot was due solely to advancement of z_{\max} , and the behavior can be explained using a mass-conservation argument. The observed behavior indicates that approximately two-thirds of the domain width is stagnant (not conducting air), forcing the remaining third to compensate by moving three times faster. This preferential advancement of the foremost finger is pre-

dicted by the stability analysis given in Sec. II A 2, and has been observed in other viscous fingering studies [2,5].

For the capillary fingering simulations ($Bo^* = -0.006$ and -0.008), Δz increased at the prescribed flux rate of the system on average, but with much more scatter than in the viscous fingering case. Z_{\max} increased relatively linearly at approximately twice the prescribed flux, while z_{\min} exhibited a stepwise increase. The fluid-fluid contact line periodically detached from clusters of liquid, trapping them behind the advancing front and creating discontinuous jumps in z_{\min} . In contrast to the viscous fingering simulations, in which the increase in z_{\max} was due to the growth of one dominant finger, the capillary fingering simulations featured the growth of two or more fingers at similar rates. This contributes to the decreased slope of the z_{\max} line relative to the prescribed flux; in this case, approximately half of the domain was conductive.

An alternative explanation for the observed front width evolution is based on a force-balance perspective. For the viscous fingering case, $\Delta z(t)$ is wholly determined by $z_{\max}(t)$ since z_{\min} remains pinned at or near the inlet $z_{\min}(0)$. $Z_{\max}(t)$ is controlled by a combination of the characteristic fluid morphology (a few dominant, narrow fingers control the flow) and to a lesser extent the spatial distribution of pore sizes, which determines which portions of the domain are most conductive. For the capillary fingering case, $\Delta z(t)$ is affected by both z_{\min} and z_{\max} . $Z_{\max}(t)$ behaves as in the viscous fingering case, but since the fingers are wider and more numerous, a larger fraction of the domain is conductive. $Z_{\min}(t)$, however, is dependent only on the spatial distribution of pore sizes in the domain. Trailing portions of the front will advance when all other portions are pinned by small pore throats. Therefore, the behavior of Δz is a composite parameter that depends on both the flow regime and the porous medium under consideration. This suggests that the “characteristic” slopes shown in Fig. 6(a) are likely to be dependent on the medium under consideration, and would vary based on spatial arrangement of pores and/or pore size distribution. This would be an interesting area for further study.

3. Front width scaling for stable fronts

We compared our results with the scaling prediction of Meheust *et al.* [10] [Eq. (4)] by analyzing the behavior of the fronts for all simulations with $Bo^* > 0$. We extracted the coordinates of the front points for each simulation from the thresholded image (see Fig. 3), and calculated the standard deviation of the z coordinates. This provides a statistical description of the width of the front, which is a measure of the instability of the system. In general, we observe that front standard deviation increases as Bo^* decreases toward zero. Specifically, Fig. 7 shows comparison of our data with Meheust *et al.*'s [10] prediction. Because the data showed excellent agreement with the exponent predicted by Eq. (4) [$-\nu/(1+\nu) = -4/3^*(1+4/3) = -0.571$], we used only the coefficient $\sigma/W_p a$ as a fitting parameter. The fitted value of the coefficient was higher but on the same order of magnitude as the predicted value (predicted 0.026, fitted 0.064).

B. Effective diffusion coefficient results

We obtained effective diffusion coefficient values using the LBM according to the methodology outlined in Sec.

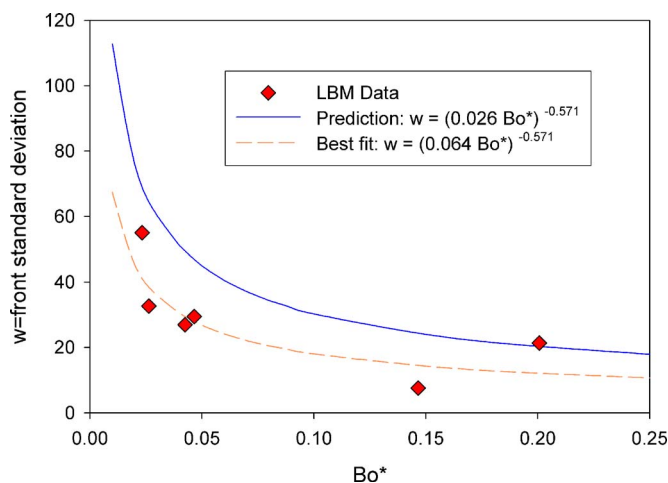


FIG. 7. (Color online) Comparison of LBM data for $Bo^* > 0$ with Meheust *et al.*'s [10] scaling law for stable fronts [Eq. (4)]. Fitted curve uses theoretical value of the exponent and fitted coefficient.

III D. Three series of simulations were performed: one using fluid configurations from a viscous fingering drainage simulation [$Bo^* = -0.12$, Fig. 5(a)], one from a capillary fingering simulation [$Bo^* = -0.006$, Fig. 5(d)], and one from a stable drainage simulation [$Bo^* = 0.15$, Fig. 5(f)]. Diffusion was simulated in domains from each series with liquid contents ranging from zero to full saturation ($\theta = n = 0.7$). The geometry of the diffusion simulations was as follows: constant concentration boundaries were fixed on the left and right sides of the medium, producing a gradient perpendicular to the flow direction of the drainage simulations [Fig. 3(d)]. This allowed gas diffusion to occur across the continuous air-filled region of the domain. The degree of continuity of the air phase (or amount of trapping of the liquid phase) determined the resistance to diffusive gas flux and therefore the magnitude of the effective diffusion coefficient.

Relative diffusion coefficients as a function of water content for three representative series of simulations are shown in Fig. 8. (The relative diffusion coefficient D_{rel} is equal to the effective diffusion coefficient scaled by the value in open air.) For the stable drainage case, D_{rel} decreases linearly with increasing volumetric liquid content. This is expected due to the regular geometry of the advancing front; each successive time step produces an almost perfectly rectangular air-filled region. Since the solid particles are uniformly distributed in the domain, the porosity of each region is the same, and therefore as the liquid content decreases, the diffusive flux increases linearly.

In contrast, for the viscous fingering case, even a small amount of residual liquid content has a large effect on D_{rel} . As the water content drops below full saturation, the continuity of the air phase increases very little, since air invades in fingers and leaves large “antifingers” of liquid still in place. The antifingers persist throughout the drainage process, and remain in place even at low water content. This is the mechanism responsible for the large reduction in D_{rel} relative to the stable displacement case observed in Fig. 8. This effect is most important at intermediate liquid contents

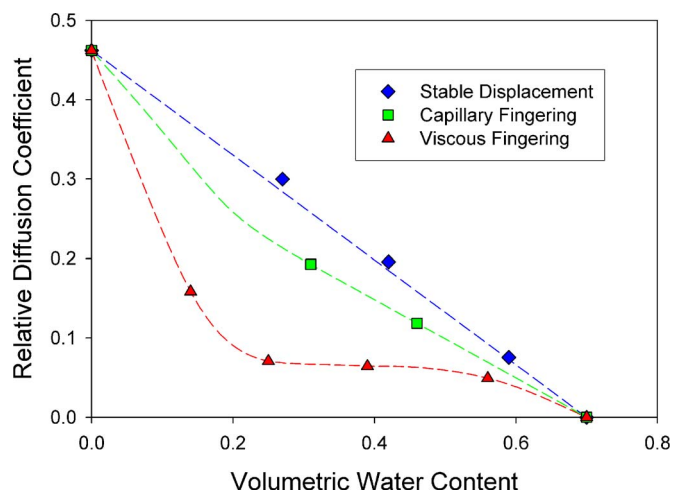


FIG. 8. (Color online) Relative diffusion coefficient as a function of water content for three representative simulations. Note the significant reduction in diffusion coefficient for the viscous fingering domain relative to stable displacement.

and becomes negligible at zero and full saturation. In our 2D porous medium, a maximum reduction of 76% in D_{rel} occurs at $\theta \approx 0.25$.

The capillary fingering case gives results intermediate between viscous fingering and stable displacement. The lower drainage velocity gives rise to less instability than is observed in the viscous fingering simulation, and therefore the fingering effects on diffusion are not as pronounced. Also, as the least advanced portion of the front z_{min} advances in a stepwise fashion as shown in Fig. 6(b), it leaves an open portion of the domain with no resistance to flow. The maximum measured reduction in D_{rel} relative to the stable value occurs at $\theta = 0.31$ with a reduction of 25%.

V. CONCLUSIONS

We have studied immiscible flow morphology in a two-dimensional porous medium using the LBM. We found good agreement between the morphology exhibited in our small-scale simulations with that of published experimental results as a function of dimensionless parameter $Bo^* = Bo - Ca$. Subsequent simulations of gaseous diffusion through the air-filled portion of the porous medium at varying water contents for two different flow morphologies showed significant reductions in the relative diffusion coefficient in the case of viscous fingering relative to the stable drainage case, and lesser reductions for capillary fingering relative to stable drainage.

The limited domain size and the 2D nature of the simulations are obvious limitations of this study, reflecting the balance between maintaining computational efficiency and capturing the essential physical behavior of the system. Relatively small computational domains increase the sensitivity of results to dominant geometrical features in the simulated porous medium, such as high-permeability zones. Simulations in 2D eliminate connectivity in the third dimension; hence liquid fingers present complete obstacles to gas

diffusion. In a 3D system, gas flux could proceed behind or in front of a liquid finger, lessening the effect on the measured diffusion coefficient. Therefore, we would expect the observed reductions in diffusion coefficient in fingering domains to be less drastic in a real system than in our 2D simulations.

In the context of reduced-gravity plant growth modules, our findings point to the need for reliable information about liquid configuration, as this has a significant effect on the potential for development of hypoxic conditions in the root zone. In a reduced gravity environment with $g \approx 0$, flow systems would be operating at negative Bo^* values resulting in instability of air-liquid interfaces. The minimization of fingering effects on macroscopic diffusive gas flux hinges on

reducing instabilities, which implies reducing the capillary number of a flow system.

In conclusion, this work demonstrates that LBM accurately simulates flow processes in porous media under a range of flow conditions, and contributes to an enhanced understanding of the role of dynamic fluid behavior on diffusive transport in partially saturated porous media.

ACKNOWLEDGMENTS

We wish to thank M.C. Sukop for helpful discussions, and we gratefully acknowledge the support of NASA under Grants No. 01-OBPR-01-009 and No. NAG 9-1399.

-
- [1] R. Lenormand and C. Zarcone, Phys. Rev. Lett. **54**, 2226 (1985).
- [2] R. Lenormand, E. Touboul, and C. Zarcone, J. Fluid Mech. **189**, 165 (1988).
- [3] G. M. Homsy, Annu. Rev. Fluid Mech. **19**, 271 (1987).
- [4] S. Hill, Chem. Eng. Sci. **1**, 247 (1952).
- [5] J.-D. Chen and D. Wilkinson, Phys. Rev. Lett. **55**, 1892 (1985).
- [6] J. V. Maher, Phys. Rev. Lett. **54**, 1498 (1985).
- [7] K. J. Måløy, J. Feder, and T. Jøssang, Phys. Rev. Lett. **55**, 2688 (1985).
- [8] G. Chen, M. Taniguchi, and S. P. Neuman, Nuclear Regulatory Commission Report NUREG/CR-6308 (1995).
- [9] B. Berkowitz and R. P. Ewing, Surv. Geophys. **19**, 23 (1998).
- [10] Y. Méheust, G. Løvoll, K. J. Måløy, and J. Schmittbuhl, Phys. Rev. E **66**, 051603 (2002).
- [11] J. F. Gouyet, M. Rosso, and B. Sapoval, Phys. Rev. B **37**, 1832 (1988).
- [12] S. B. Jones, D. Or, and G. E. Bingham, Vadose Zone J. **2**, 602 (2003).
- [13] J. F. Chau, D. Or, and M. C. Sukop, Water Resour. Res. **41**, W08410 (2005).
- [14] P. Moldrup, T. Olesen, J. Gamst, P. Schjonning, T. Yamaguchi, and D. E. Rolston, Soil Sci. Soc. Am. J. **64**, 1588 (2000).
- [15] X. Shan and H. Chen, Phys. Rev. E **49**, 2941 (1994).
- [16] L.-S. Luo, Phys. Rev. E **62**, 4982 (2000).
- [17] F. M. Van Kats and P. J. P. Egberts, Transp. Porous Media **37**, 55 (1999).
- [18] H. Fang, Z. Wang, Z. Lin, and M. Liu, Phys. Rev. E **65**, 051925 (2002).
- [19] A. Yamamoto and M. Suzuki, J. Chem. Eng. Jpn. **35**, 944 (2002).
- [20] J. G. Zhou, Int. J. Mod. Phys. A **13**, 1135 (2002).
- [21] M. Hilpert, J. Math. Biol. 10.1007/s00285-005-0318-6 (2005).
- [22] M. C. Sukop and D. Or, Water Resour. Res. **40**, W01509 (2004).
- [23] B. R. Munson, D. Young, and T. H. Okiishi, *Fundamentals of Fluid Mechanics* (Wiley, Ames, IA, 2002).
- [24] S. J. Chen, D. Martínez, and R. Mei, Phys. Fluids **8**, 2527 (1996).
- [25] C. Adler, B. Boghosian, E. G. Flekkoy, N. Margolus, and D. H. Rothman, J. Stat. Phys. **81**, 105 (1995).
- [26] T. Podgorski, J.-M. Flesselles, and L. Limat, Phys. Rev. Lett. **87**, 036102 (2001).
- [27] D. Or and T. Ghezzehi, Transp. Porous Media (to be published).
- [28] J. Bico and D. Quere, J. Colloid Interface Sci. **243**, 262 (2001).
- [29] G. Su, J. T. Gellar, J. R. Hunt, and K. Pruess, Vadose Zone J. **3**, 592 (2004).